Draft version February 20, 2022
Typeset using LaTeX **twocolumn** style in AASTeX62

Constraining Dark Energy With Stacked Concave Lenses

Fuyu Dong,[1] Jun Zhang*,[1] Yu Yu,[1] Xiaohu Yang,[1,2] HeKun Li,[1] Jiaxin Han,[1,3] Wentao Luo,[1] Jiajun Zhang,[1] and Liping Fu[4]

[1] *Department of Astronomy, School of Physics and Astronomy, and Shanghai Key Laboratory for Particle Physics and Cosmology, Shanghai Jiao Tong University, Shanghai 200240, China*

[2] *IFSA Collaborative Innovation Center, and Tsung-Dao Lee Institute, Shanghai Jiao Tong University, Shanghai 200240, China*

[3] *Kavli IPMU (WPI), UTIAS, The University of Tokyo, Kashiwa, Chiba 277-8583, Japan*

[4] *The Shanghai Key Lab for Astrophysics, Shanghai Normal University, Shanghai 200234, China*

ABSTRACT

Low density regions are less affected by the nonlinear structure formation and baryonic physics. They are ideal places for probing the nature of dark energy, a possible explanation for the cosmic acceleration. Unlike void lensing, which requires identifications of individual voids, we study the stacked lensing signals around the low-density-positions (LDP), defined as places that are devoid of foreground bright galaxies in projection. The method allows a direct comparison with numerical results by drawing correspondence between the bright galaxies with halos. It leads to lensing signals that are significant enough for differentiating several dark energy models. In this work, we use the CFHTLenS catalogue to define LDPs, as well as measuring their background lensing signals. We consider several different definitions of the foreground bright galaxies (redshift range & magnitude cut). Regarding the cosmological model, we run six simulations: the first set of simulations have the same initial conditions, with $w_{de} = -1, -0.5, -0.8, -1.2$; the second set of simulations include a slightly different ΛCDM model and a w(z) model from Zhao et al. (2017). The lensing results indicate that the models with $w_{de} = -0.5, -0.8$ are not favored, and the other four models all achieve comparable agreement with the data.

Keywords: Gravitational lensing: weak - Cosmology: large-scale structure of universe - Cosmology: dark energy - Galaxies: halos

1. INTRODUCTION

The acceleration of the cosmic expansion remains to be a mystery today (Riess et al. 1998; Perlmutter et al. 1999; Weinberg et al. 2013; Komatsu et al. 2014; Planck Collaboration et al. 2014). It is not yet clear if it is necessary to go beyond the simplest ΛCDM model by introducing a nontrivial equation of state $w(z)$ for dark energy (Huterer & Turner 1999). Recently, from the baryon acoustic oscillation measurement of the BOSS data, there has been intriguing evidence showing a deviation of $w(z)$ from -1 (Zhao et al. 2017). It is desirable to test the nature of dark energy with alternative cosmological probes. We propose to do so with the weak lensing effect around low density regions.

Low density regions have the advantages of being much less affected by nonlinear evolution and baryonic physics. They are likely the ideal places to test dark energy models with weak lensing. Previous efforts largely focus on the lensing effect of voids, a typical type of low density region that is devoid of matter over a significant cosmic volume.

A major challenge of void lensing is about identifying the voids. Current void-finding algorithms are mostly based on the distribution of galaxies with spectroscopic redshifts. Sánchez et al. (2017) has summarized these algorithms into several groups: Watershed Void Finders (Platen et al. 2007; Neyrinck 2008; Lavaux & Wandelt 2012; Nadathur et al. 2015), growth of spherical underdensities (Hoyle & Vogeley 2002; Colberg et al. 2005; Padilla et al. 2005; Ceccarelli et al. 2006; Li 2011), hybrid methods (Jennings et al. 2013), dynamical criteria (Elyiv et al. 2015), and Delaunay Triangulation (Zhao et al. 2016). There are however three main shortcomings in traditional ways of doing void lensing: 1. void centers cannot be unambiguously identified due to their intrin-

*betajzhang@sjtu.edu.cn

sically irregular shapes, making it difficult to precisely predict or understand the stacked void lensing signals with a physical model; 2. spectroscopic galaxy surveys are generally expensive, and suffer from complicated influences from the selection effects; 3. due to the limited number density of voids and the scatter of their sizes, the stacked lensing signals do not yet have a high significance.

More recently, there is a trend to study the lensing effect of low density regions defined by the projected galaxy distributions (Clampitt & Jain 2015; Sánchez et al. 2017; Gruen et al. 2016; Friedrich et al. 2018; Gruen et al. 2018; Barreira et al. 2017; Davies et al. 2018; Brouwer et al. 2018). Comparing to void lensing, these new methods only need photo-z information, and the stacked lensing signals generally have much higher significance. For example, Gruen et al. (2016) use a photometrically selected luminous red galaxy sample (redMaGiC) as the foreground galaxies in their paper. By dividing the sky into cells, they assign each cell a weighted and smoothed galaxy count. They do shear measurements around cells with different galaxy counts using DES lensing catalogue. Their follow-up works can be found in Gruen et al. (2018); Friedrich et al. (2018), in which a complete cosmological analysis is presented within the LCDM models.

Our approach has similarities to their method, but also with differences. We consider these low density positions ("LDPs"), which is defined by excluding the foreground bright galaxies from the sky with a critical radius in projection. This is a direct way to define the low density regions, without defining the galaxy density map. These positions can be similarly defined in N-body simulations by drawing correspondence between the foreground bright galaxies and halos/subhalos through, e.g., subhalo abundance matching (SHAM, e.g., Vale & Ostriker 2004). These operations are straightforward to realize, and enable us to directly compare the stacked lensing signals around LDPs with the simulation predictions. The motivation of this paper is to differentiate several different dark energy models through this type of comparison.

This paper is organized as follows: In §2, we introduce the basic theory of weak lensing, and the method for stacking the lensing signals from low density regions in both observations and numerical simulations; §3 shows our main results for several different dark energy models; §4 gives our conclusion and discussions about related issues.

2. METHOD

2.1. *Overview*

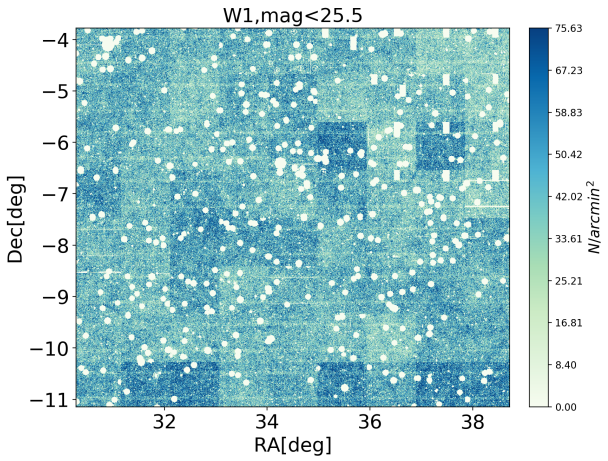

Figure 1. Source distribution in W1 from CFHTLenS catalogue with apparent magnitude $\mathrm{mag_i} < 25.5$. The empty areas in this map are masked out for bright stars.

The background tangential shear is related to the stacked excess surface density of the foreground (see, e.g., Peacock (1999)):

$$\Delta\Sigma(\mathrm{R}) \equiv \Sigma_{\rm cr}(\mathrm{z_l}, \mathrm{z_s})\langle\gamma_{\rm t}\rangle(\mathrm{R}) = \overline{\Sigma}(<\mathrm{R}) - \overline{\Sigma}(\mathrm{R}), \quad (1)$$

where R is the distance to the center, and $\Sigma_{\rm cr}(\mathrm{z_l}, \mathrm{z_s})$ is the critical surface density in comoving unit, which is defined as:

$$\Sigma_{\rm cr}(\mathrm{z_l}, \mathrm{z_s}) = \frac{\mathrm{c}^2}{4\pi\mathrm{G}} \frac{\mathrm{D_A}(\mathrm{z_s})}{\mathrm{D_A}(\mathrm{z_l})\mathrm{D_A}(\mathrm{z_l}, \mathrm{z_s})(1+\mathrm{z_l})^2}, \quad (2)$$

where $\mathrm{z_s}$ and $\mathrm{z_l}$ are the redshifts of the source and the lens respectively ($\mathrm{z_l} < \mathrm{z_s}$). $\overline{\Sigma}(<\mathrm{R})$ is the meaning surface density within R, and $\overline{\Sigma}(\mathrm{R})$ is the surface density at R. $\mathrm{D_A}$ refers to the angular diameter distance. By stacking the background shear signals, Eq.(2) allows us to probe the average surface density profile around the foreground objects (e.g., galaxies, cluster centers, void centers, etc.) directly, with an enhanced significance and better circular symmetry.

There are in principle no restrictions on how one defines the foreground positions as long as they are physically meaningful. For our purpose of studying the properties of dark energy, we consider stacking the shear signals around LDPs, which are simply defined as places that are away from foreground bright galaxies (within a certain narrow redshift range) by more than a critical distance in projection. LDPs defined in such a way generally point to low-density regions. They provide abundant foreground positions for shear-stacking, leading to highly significant lensing signals, as shown in the rest of the paper.

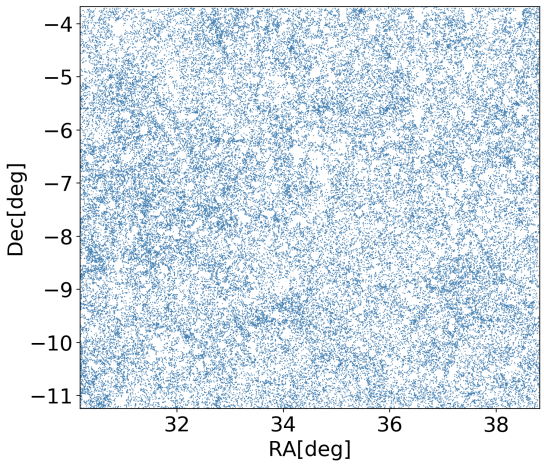

Figure 2. The panel shows galaxy distribution in W1 with absolute magnitude $\mathrm{Mag_i} < -21.5$, $0.335 < \mathrm{z} < 0.535$.

2.2. *Observational Data*

We use the shear catalogue from CFHTLenS (Canada-France-Hawaii Telescope Lensing Survey)[1], which comprises 171 pointings with an effective survey area of about 154 deg^2. The CFHTLenS data set is based on the Wide part of CFHTLS carried out in four patches: W1,W2,W3,W4. It has deep photometry in five broad bands $u^*g'r'i'z'$ (also the y' band as a supplement to i' band) and limiting magnitude in the i' band of $i'_{\mathrm{AB}} \sim 25.5$. Heymans et al. (2012) presents the CFHTLenS data analysis pipeline, which summarizes the weak lensing data processing with THELI (Erben et al. 2013), shear measurement with Lensfit (Miller et al. 2013), and photometric redshift measurement with the Bayesian photometric redshift code (Hildebrandt et al. 2012).

For each galaxy in the shear catalogue, we are provided with an inverse-variance weight w, the shape measurement $\epsilon_{1,2}$, the shear correction terms from calibration, the apparent and absolute magnitudes (including extinctions and Magnitude error) in five band, the probability distribution function (PDF) of redshift, as well as the peak $\mathrm{z_p}$ of the PDF. The stacked shears are calculated as (Miller et al. 2013):

$$\gamma_{1,2} = \frac{\sum_{\mathrm{i}} \mathrm{w_i}(\epsilon_{\mathrm{i}(1,2)} - \mathrm{c_{i(1,2)}})}{\sum_{\mathrm{i}} \mathrm{w_i}(1+\mathrm{m_i})}, \qquad (3)$$

where $\mathrm{m_i}$ and $\mathrm{c_i}$ are the multiplicative and additive calibration terms respectively.

[1] http://cfhtlens.org

In order to generate the positions of the LDPs, we use the foreground bright galaxies above a certain absolute magnitude, so that the galaxy sample is complete in the unmasked areas. This allows us to draw correspondence between the observed galaxies and the halos in simulations, and to construct the average excess surface density profile around the LDPs in both cases for comparison. For example, Fig.1 shows the source distribution in W1 from CFHTLenS catalogue with i' band apparent magnitude less than 25.5 in the W1 area. The differences in number densities across different fields is quite obvious. The empty areas in this map are masked out for bright stars. If only the bright galaxies are kept, the sample becomes statistically homogeneous in the unmasked areas for redshifts that we are interested in. As an example, we show the distribution of galaxies with $0.335 < \mathrm{z} < 0.535$ and i'-band absolute magnitude $\mathrm{Mag_i} \leq -21.5$ in Fig.2.

The positions of the LDPs are identified through the following procedures:

1. Generating the LDP candidates

First of all, we require each foreground galaxy to be brighter than a critical absolute magnitude $\mathrm{Mag_c}$ in the i'-band, with redshift between [$\mathrm{z_m}$-0.1, $\mathrm{z_m}$+0.1], where $\mathrm{z_m}$ is the median redshift. We circle around each foreground galaxy with radius $\mathrm{R_s}$. Regions within the radius are removed, and the remaining positions are the candidates for LDPs. In principle, there are infinite LDPs. In this work, for simplicity, we put the LDPs on a uniform grid, with the grid size equal to 0.37 arcmin. The thickness of the redshift slice is set to 0.2 considering the typical redshift dispersion σ_z[2]. $\mathrm{R_s}$[3] here is set to 1 or 1.5 arcmin in order to generate enough LDPs. The $\mathrm{Mag_c}$ here refers to the critical magnitude in one particular LCDM model (CW1 in §2.3). For other cosmologies, we use almost the same foreground galaxy sample[4]. To ensure a clean and complete foreground galaxy sample for generating LDPs, we make three constraints here:

[2] We fit each galaxy redshift PDF with a gaussian form to gain the redshift dispersion σ_{z}, which is typically around ∼0.1.

[3] There are no restrictions on the way to remove galaxies, and a lot of tricks can be done in this process. For example, each galaxy can be assigned with an individual $\mathrm{R_s}$, according to its luminosity or mass. It is also a reasonable way to fix $\mathrm{R_s}$ for all the galaxies, as done here.

[4] We always select the same amount of brightest galaxies as the foreground galaxies. For different cosmologies, the rank of the galaxy brightness may change. For example, for a given apparent magnitude at redshift $\mathrm{z_1}$ and $\mathrm{z_2}$, it is possible that the absolute magnitude $\mathrm{Mag(z_1, w_{de1}) > Mag(z_2, w_{de1})}$ but $\mathrm{Mag(z_1, w_{de2}) < Mag(z_2, w_{de2})}$, due to the change of the distance-redshift relation. However, this rarely happens for cosmologies we use.

a) We only use sources with star_flag = 0 to decrease the star contaminations(but not vanished). Overall, the fraction of sources with star_flag = 1 is around 3%. The ratio becomes $\sim$ 20% for galaxies satisfying $0.335 < z < 0.535$ and $Mag_i < -21$. In general, the ratio changes with magnitude and redshift.

b) Galaxies which have two or more close height peaks in redshift PDF are removed to reduce the redshift uncertainty. Most of these sources are actually stars. It further remove $\sim$ 3% sources for galaxies under condition star_flag = 0, Mag_i <-21, $0.335 < z < 0.535$. This ratio changes with magnitude and z_m.

c) We also remove galaxies with absolute magnitude Mag_i <-99 in the original catalogues, which indicates problems in the measurement. This corresponds to the removal of 10 percent additional sources. In §4, we show that these sources generally yield low galaxy-galaxy lensing signals, therefore should not be the foreground galaxies we consider.

After the above selection of galaxies, our i-band luminosity function is consistent with the CFHTLS-DEEP-SURVEY luminosity function derived by Ramos et al. (2011).

2. Generating the mask maps

We use the CFHTLenS Mosaic mask files(Erben et al. 2013) in this step. In order to produce the mask maps in (ra, dec) units, we generate the uniform grids for W1-4 firstly. Then we apply VENICE[5] with these official files to accurately mask these positions near the mask boundaries.

3. Finding out the LDPs from candidates

Some of the candidate LDPs generated in step 1 should be removed if they are close to the masked regions. We require the ratio of the masked area to πR_s^2 around each candidate LDP to be less than 10 percent. To get rid of the survey edge effects, we also remove the LDPs whose distances from the edges of the survey area are less than R_s.

For LDPs generated through steps 1 to 3, we measure their stacked excess surface density $\Delta\Sigma(R)$ using background galaxies, and compare it with predictions of different cosmological simulations introduced in the next section.

2.3. *Simulation*

[5] https://github.com/jcoupon/venice

Table 1. Simulation parameters.

Simulation	w_{de}	σ_8	Ω_c	Ω_b	h	n_s
CW1	-1	0.85	0.223	0.045	0.71	1
CW2	-0.5	(0.633)	0.223	0.045	0.71	1
CW3	-0.8	(0.789)	0.223	0.045	0.71	1
CW4	-1.2	(0.893)	0.223	0.045	0.71	1
Simulation	w_{de}	A_s	Ω_c	Ω_b	h	n_s
WZ1	-1	2.2e-9	0.2568	0.0485	0.679	0.968
WZ2	w(z)	2.2e-9	0.24188	0.04525	0.702	0.966

We run two sets of simulations named as CW (standing for constant w) and WZ (referring to w as a function of z), the parameters of which are given in table 1. In all of our simulations, we set $\Omega_{de} + \Omega_c + \Omega_b = 1$. 2LPT and Gadget2 are used to create initial conditions and run the simulations (Springel & Hernquist 2002; Springel 2005). Both CW and WZ simulations are run from initial redshift 72 with particle number 1024^3 and boxsize 600 Mpc/h. We use the FoF group finder to find out the halos, and the subhalo finder HBT (Han et al. 2012) to find the subhalos.

i) For CW1, we produce the initial condition following parameters ($\sigma_8 = 0.85$,$\Omega_c = 0.223$, $\Omega_b = 0.045$, $n_s = 1$). For CW2,3,4 the same initial conditions are used, with updated H(z) for different w_{de} model in Gadget2. The value of σ_8 in the 4 simulations reduces with increasing w.

ii) For the second set, we adopt the best fit cosmological parameters from Zhao et al. (2017) for ΛCDM and dynamical dark energy w(z) model, and use CAMB (Lewis et al. 2000) to generate the initial power spectrum for the simulation.

The LDPs in simulations are defined in the following way:

1. Connecting halos/subhalos with galaxies through SHAM

There are different methods in literature to populate galaxies in dark matter halos/subbhalos: either through the halo occupation distribution and conditional luminosity function models (Jing et al. 1998; Berlind & Weinberg 2002; Yang et al. 2003; Zheng et al. 2005; van den Bosch et al. 2007; Zehavi et al. 2011; Leauthaud et al. 2011; Yang et al. 2012; Rodríguez-Puebla et al. 2015; Zu & Mandelbaum 2016; Guo et al. 2016; Rodríguez-Puebla et al. 2017; Guo et al. 2018), or via subhalo abundance matching processes (e.g. Vale & Ostriker 2004; Conroy et al. 2006; Vale & Ostriker 2006; Conroy et al. 2009; Behroozi et al. 2010; Guo et al. 2010; Simha et al. 2012; Hearin et al. 2013; Guo & White 2014; Chaves-Montero et al. 2016; Wechsler & Tinker 2018; Yang et al. 2018).

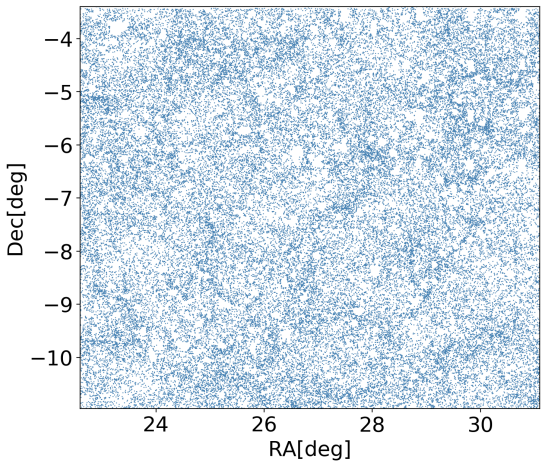

Figure 3. The figure shows galaxy distribution from one sub-area of CW1 simulation for $\mathrm{Mag_i}$ <-21.5, $0.335 < z < 0.535$.

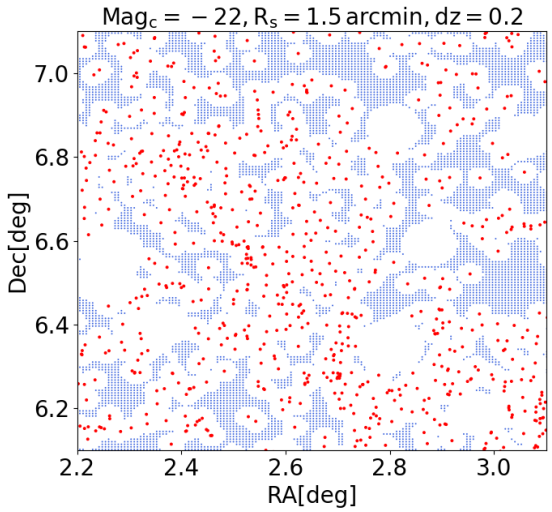

Figure 4. An example showing the LDP positions (in blue) in our CW1 simulation with $\mathrm{Mag_c}$=-22, $\mathrm{R_s}$=1 arcmin, $\mathrm{z_m} = 0.435$ and the slice thickness dz=0.2. Red points are the locations of the mock galaxies. The white regions are either the masked areas or the neighborhood of the mock galaxies.

In this work, for simplicity, we use the SHAM method to generate mock galaxy catalogs.

To make the galaxy-subhalo abundance match, we first put the simulation box along the line of sight at redshift $\mathrm{z_m}$. Then we use galaxies in the redshift range of $[\mathrm{z_m} - 0.1, \mathrm{z_m} + 0.1]$ to match the halos/subhalos in the simulation. We adopt the masks of observation in the simulation in order to mimic the mask distribution in observation. Assuming brighter galaxies are formed

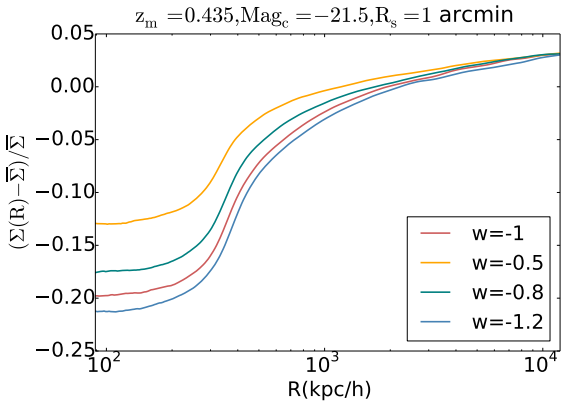

Figure 5. The curve shows the normalized surface density $(\Sigma(\mathrm{R}) - \overline{\Sigma})/\overline{\Sigma}$ around LDPs defined with $\mathrm{Mag_c} = -21.5$, $\mathrm{R_s}$ =1 arcmin, $\mathrm{z_m}$ =0.435 and dz=0.2 for CW1,2,3,4, where $\overline{\Sigma}$ is the mean surface density around the random points.

in bigger halos/subhalos, the connection between the halos/subhalos and galaxies are built up by comparing the number of halos/subhalos with mass greater than M to the number of galaxies with luminosity greater than L:

$$\int_{\mathrm{L}}^{\infty} \phi(\mathrm{L})\mathrm{dL} = \int_{\mathrm{M}}^{\infty} [\mathrm{n_h}(\mathrm{M}) + \mathrm{n_{sh}}(\mathrm{M})]\mathrm{dM}, \qquad (4)$$

where

$$\mathrm{M} = \begin{cases} \mathrm{M_{acc}}, & \text{subhalos} \\ \mathrm{M_z}, & \text{distinct halos}, \end{cases} \qquad (5)$$

where $\mathrm{n_h}/\mathrm{n_{sh}}$ is the number of halos/subhalos, and $\mathrm{M_{acc}}$ is the mass at the last epoch when the subhalo is a distinct halo. It is commonly used in the SHAM models since it is closely related to the halo merger history. $\mathrm{M_z}$ is the halo mass at redshift z.

We also add some scatters to the redshifts and luminosities of our mock galalxies to better mimic the real situation. Firstly, the redshift dispersion measured in §2.2 is added to halos/subhalos to randomly move their positions in redshift space. We also update the absolute magnitudes of mock galaxies according to their redshift errors. Secondly, we introduce an additional mass uncertainty of the order $\sigma_{\mathrm{lgM}} = 0.3$ to halos/subbhalos to mimic the dispersion in the galaxy-halo/subhalo relation. We find that, the final results are not sensitive to the value of σ_{lgM}. We show an example of the galaxy distribution in CW1 simulation in Fig.3, which looks quite similar to that shown in Fig.2 for real galaxies.

2. Generating the LDPs

After we generate mock galaxy catalogues, candidate LDPs are generated by excluding positions within the radius R_s around bright galaxies. We also require that the ratio of the masked area to πR_s^2 around each LDP to be less than 10 percent. An example is given in Fig.4, in which the mock galaxies are marked with red color, and LDPs are marked with the blue color. The white regions are either the masked areas or the neighborhood of the mock galaxies within $R_s = 1.5$ arcmin. The average excess surface density is calculated by stacking the density profile around each LDP.

We show the normalized surface density $(\Sigma(R) - \overline{\Sigma})/\overline{\Sigma}$ around the LDPs of our four different CW simulations in Fig.5, where $\overline{\Sigma}$ is the mean surface density around the random points. The LDPs are defined by mock galaxies with $Mag_c = -21$, $R_s = 1$ arcmin, $z_m = 0.435$ and the slice thickness dz=0.2. The figure shows that a higher w corresponds to a shallower density profile.

3. RESULTS

The 2D stacked shear signals around the LDPs are shown in fig.6. The upper panel shows the original shear signals calculated with eq.(3), in which obvious shear residuals can be found. We generate random points in the un-masked regions, whose number is about ten times that of the LDPs, with the mean shear signals being $\overline{\gamma}_{\rm rand,1,2} \sim 3.65 \times 10^{-4}, 8.5 \times 10^{-4}$. After subtracting $\gamma_{\rm rand,1,2}$ from $\gamma_{1,2}$ at the corresponding positions, the shear pattern corresponding to concave lens emerges, as shown in the lower panel of the figure. The red lines show the length for shear $\gamma = 0.001$ in the figure. In making this figure and the rest of our studies, we remove the background galaxies with $\sigma_z > 0.2$ and those with significant multiple peaks in the redshift PDF to reduce the redshift contamination. In order to increase the number of background galaxies and improve the S/N, here we use galaxies in all fields with shear measurement. We have also calculated the 2D shear patterns using only fields that pass the lensing residual systematics test (shown in §4), and found similar results. Therefore, the rest of our calculations are simply based on the full shear catalogue.

More quantitatively, we compare the 1D stacked lensing signals between observation and simulation. To estimate the stacked $\Delta\Sigma(R)$ in observation, we follow the formula (9,10) in Niikura et al. (2015):

$$\langle\Delta\Sigma\rangle(\mathrm{R}) = \frac{1}{\mathrm{N}}\sum_{\mathrm{a}=1}^{\mathrm{N_c}} \sum_{\mathrm{s_a}:\left|\lg\left(\frac{\mathrm{R_{s_a}}}{\mathrm{R}}\right)\right|<\Delta} \mathrm{w(a,s_a)}\Sigma_{\mathrm{cr(a)}}\epsilon_{\mathrm{(s_a)+}}(\mathrm{R_{s_a}}), \tag{6}$$

where N_c is the number of LDPs, 2Δ is the bin size on the logarithmic scale, $\epsilon_{(s_a)+}$ is the tangential ellipticity

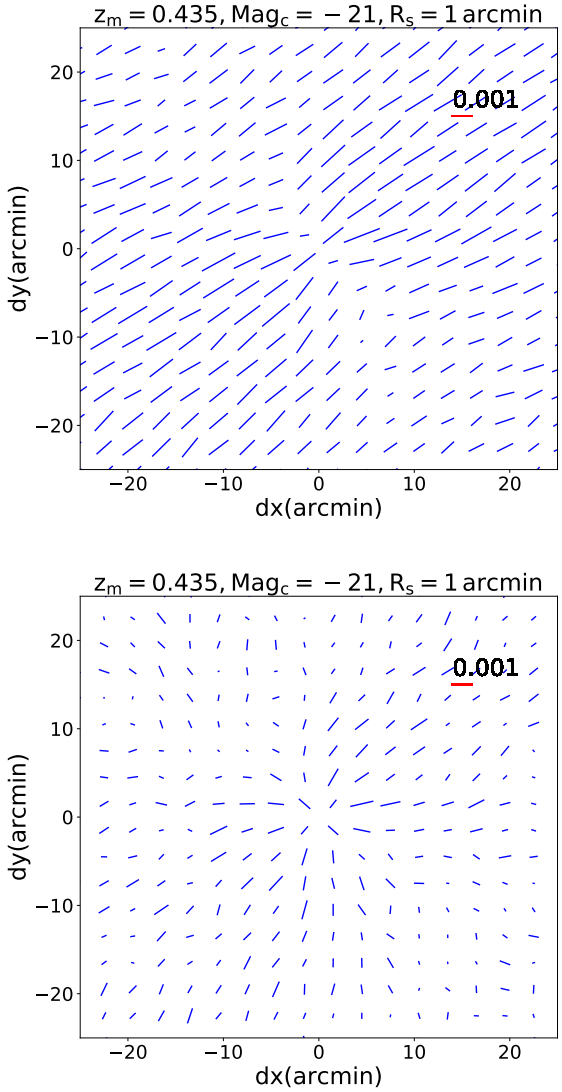

Figure 6. The 2D stacked lensing signals around the LDPs using the whole CFHTLenS shear catalogue. The upper panel shows the original result, and the lower panel shows results after subtracting the average residual $\overline{\gamma}_{1,2}$. The red line represents the shear strength of 0.001.

of the s_a-th background galaxy for the a-th LDP, R is the average radius of the background galaxies in that radial bin, and N is the normalization factor:

$$\mathrm{N} = \sum_{\mathrm{a}=1}^{\mathrm{N_c}}\sum_{\mathrm{s_a}} \mathrm{w(a,s_a)}\,. \tag{7}$$

We only use background galaxies with $z_s \geq z_l + 0.1$ when calculating $\Delta\Sigma(z_l, z_s)$, concerning the fact that both foreground and background galaxies have redshift dispersions.

One of our main results is shown in Fig.7 with $z_m = 0.435$, $Mag_c = -21.5$, and R_s =1 arcmin. The

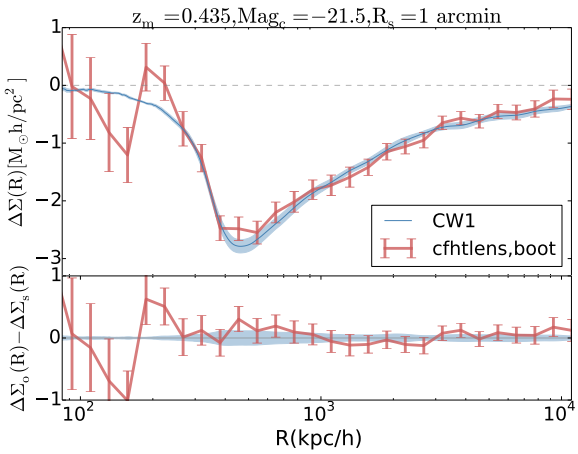

Figure 7. Results for $z_m = 0.435, Mag_c = -21.5, R_s = 1$ arcmin. The blue line is the result from the CW1 simulation. The shaded area shows the size of the cosmic variance estimated with multiple realizations using two CW1 simulations. The red line is the lensing result from the observation, with bootstrap error bars.

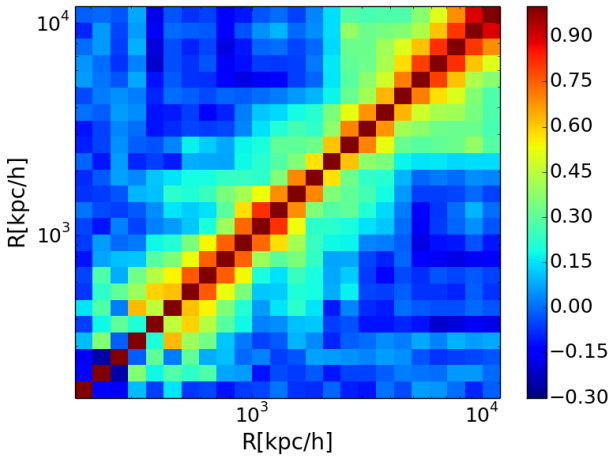

Figure 8. The normalized covariance matrix for $z_m = 0.435$, $Mag_c = -21.5$, $R_s = 1$ arcmin.

red solid line in the upper panel shows $\Delta\Sigma_o(R)$ calculated with the CFHTLenS catalogues, and the blue solid line shows $\Delta\Sigma_s(R)$ from CW1 simulation. The $\Delta\Sigma(R)$ with subscript "o" and "s" represent observational and simulation signals respectively. The lower panel is the residual $\Delta\Sigma_o(R) - \Delta\Sigma_s(R)$, which shows agreement between the simulation and observation for CW1. Two kinds of variances are given in the figure: (a) We use the simulation of Jing et al. (2007), which has the same parameters as CW1, to estimate the cosmic variance for CFHTLenS survey areas. Each of the two CW1 simulations can be used to generate 4 realizations of about 150deg^2. The variance estimated from these realizations is shown as the shaded area in the figure, with the solid blue line representing the mean value. (b) For the observational signals, the variance in red line is from bootstrap. Rather than dividing the foreground space into different subregions, we resample LDP groups that are formed by LDPs close in space to decrease the impact of masks[6]. In this way, the error bar is relatively stable even if the group size is changed for several times. To fully capture the covariance matrix, the size of the LDP group is set to be two times larger than the largest radial bin. The corresponding normalized covariance matrix is shown in Fig.8. Correlations between the neighboring radial bins can be found in the figure.

The total S/N ratio of the observational lensing signal can be calculated as:

$$\left(\frac{S}{N}\right)^2 = \sum_{i,j} \Delta\Sigma_o(\theta_i) C^{-1}_{i,j} \Delta\Sigma_o(\theta_j), \quad (8)$$
$$C^{-1}_{i,j} = \frac{N_S - N_D - 2}{N_S - 1} C^{*-1}_{i,j},$$
$$C^{*}_{i,j} = \mathrm{cov}(\Delta\Sigma_o(\theta_i), \Delta\Sigma_o(\theta_j)),$$

where the summation runs over all the radial bins. Since the sampled precision matrix $C^{*-1}_{i,j}$ is biased due to the noise in $C^{*}_{i,j}$, the unbiased estimator $C^{-1}_{i,j}$ is taken (Hartlap et al. 2007; Taylor et al. 2013). Here N_S is taken as the number of the LDP groups, and N_D is the number of the data bins. The S/N for the red line in Fig.7 is 20.473, which is significant for us to constrain cosmologies and shows the advantage of stacking signals around LDPs.

We repeat the procedures for $R_s = 1, 1.5$ arcmin, redshift bins $z_m = 0.35, 0.435, 0.512$, and Magnitude cuts $Mag_c = -21, -21.5, -22$. It enables us to make multiple comparisons with limited information. Since the apparent magnitude limit for the i'-band is higher than 24.5 on average, it allows us to make the volume-limited

[6] Given the total area for W1-4 and the largest radius R_{max} in Fig.7, the number of groups is estimated by dividing the total area by $4R^2_{max}$. The mean number of LDPs within a group is derived by dividing the total number of LDPs with the number of groups. Then we divide all the LDPs into regularly placed small cells, with each cell containing a few of LDPs. The cells are added to the groups one by one. Whenever the size of a group in a row reach $2R_{max}$, we move to another row. If the number of LDPs in a group equals to the mean number, the assignment for this group is terminated. This procedure is repeated untill the last cell is assigned to a group. In this way, the LDPs are divided into groups with similar numbers, avoiding the fluctuations due to the masking effects.

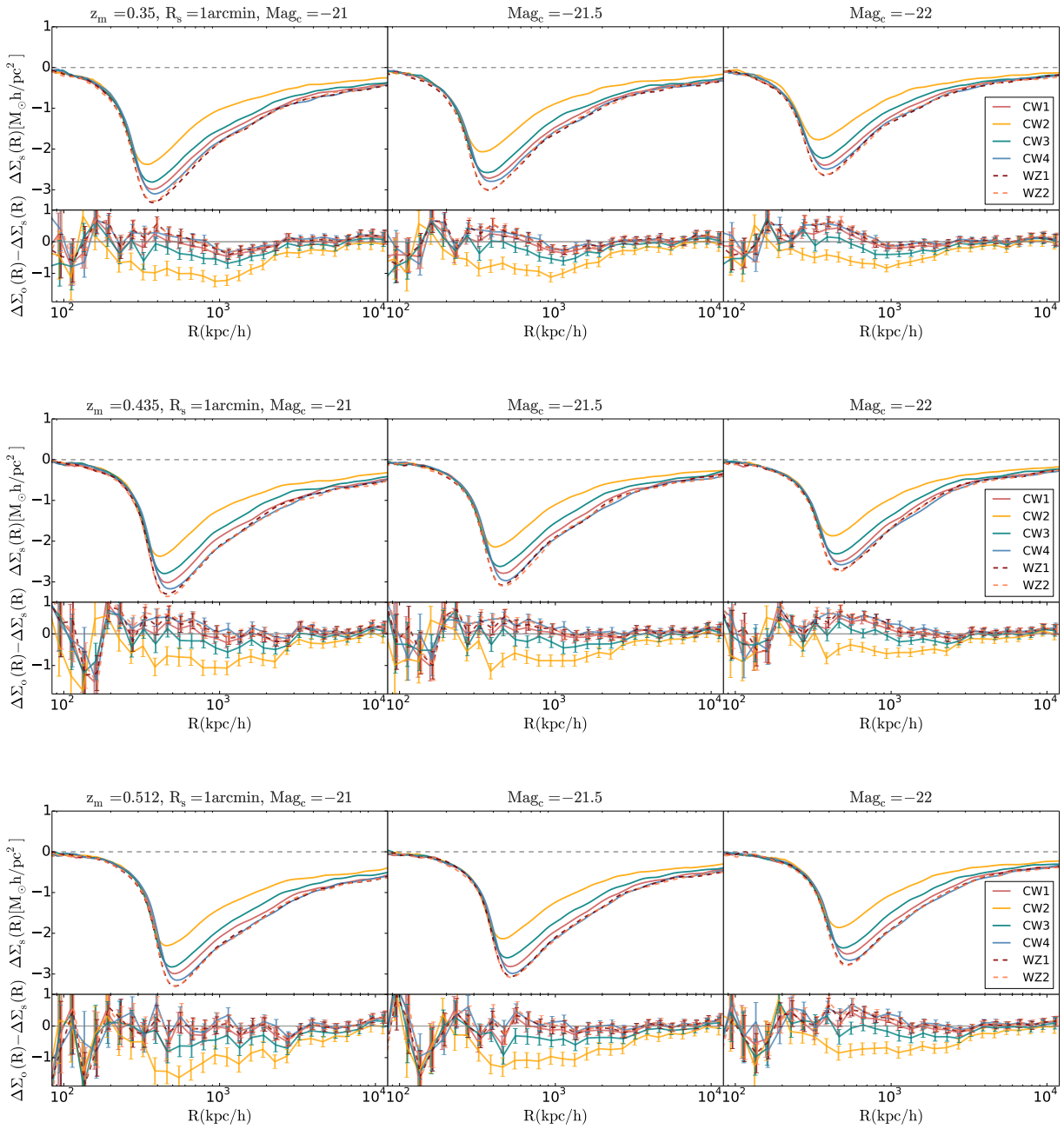

Figure 9. The average excess surface density profile around LDPs that are defined with $R_s = 1$ arcmin and different choices for the magnitude cut and redshift range. The left, middle, and right columns are for $Mag_c = -21, -21.5, -22$ respectively, and the top, middle, and bottom rows for $z_m = 0.35, 0.435, 0.512$. The upper part of each panel shows $\Delta\Sigma_s(R)$ from simulations. The lower part shows the residuals after subtracting $\Delta\Sigma_s(R)$ from $\Delta\Sigma_o(R)$.

samples for three foreground redshifts and three magnitude Mag_c cuts.

Fig.9 and Fig.10 show detailed scale dependent comparisons between simulation and observational results for R_s =1 arcmin and R_s =1.5 arcmin respectively. Panels in the horizontal direction of Fig.9 and Fig.10 are for three choices of Mag_c, and for three z_m's in the vertical direction. The arrangement of each panel is similar to that of Fig.7. One can see from the figures that there is not a single best model for all cases. It also happens that the best model in one case does not perform well at all radius scales. This situation seems to be worse for R_s =1.5 arcmin. This is likely due to the fact that the number of LDPs for R_s =1.5 arcmin is much lower than that of R_s =1 arcmin.

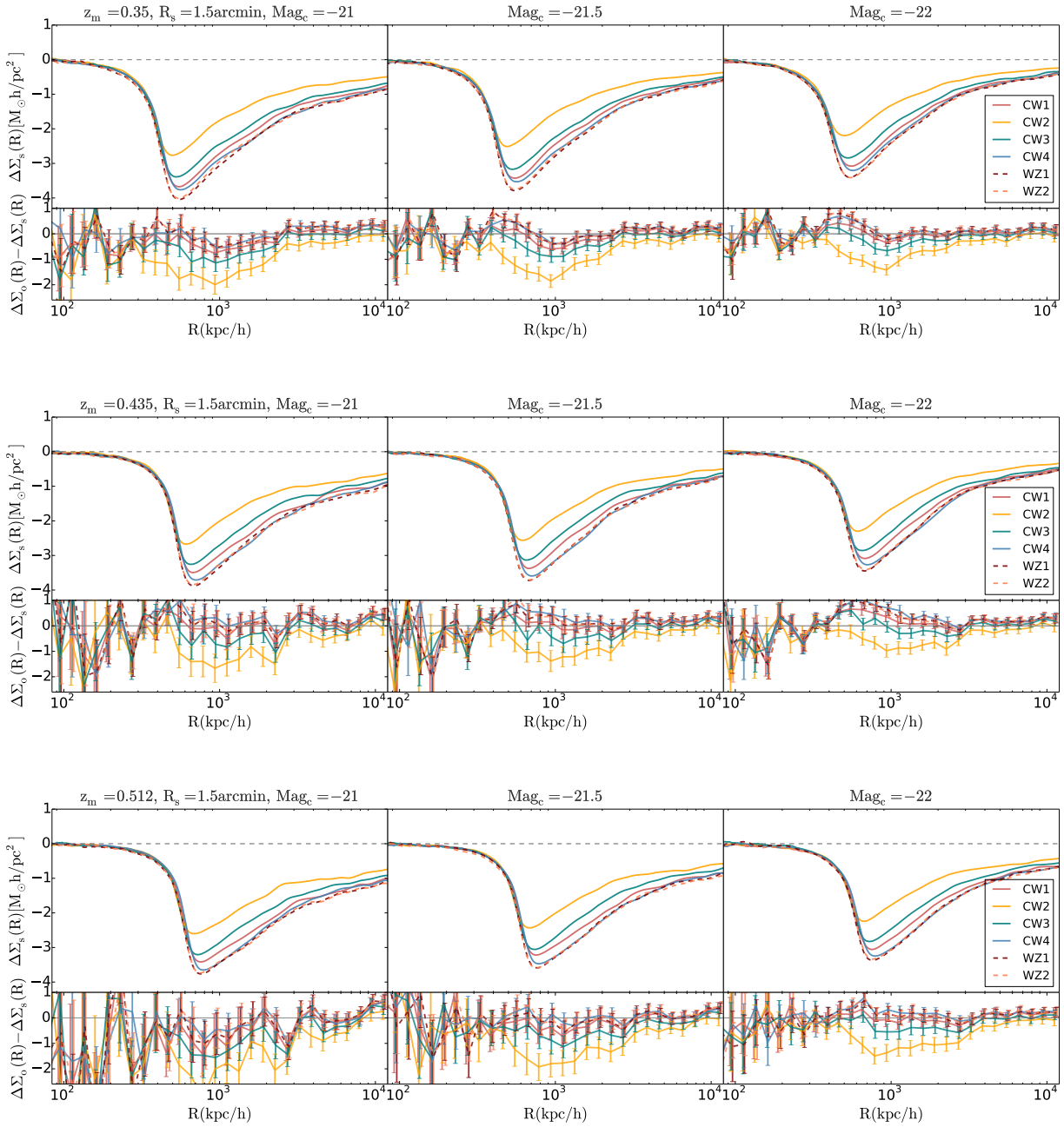

Figure 10. Similar to fig.9, but with $R_s = 1.5$ arcmin.

In order to compare the results more directly we introduce the reduced χ^2 to describe the discrepancy between observational and simulation signals:

$$\chi^2 = \frac{1}{N_{bin}} \sum_{i,j} \delta\Delta\Sigma(\theta_i) C^{-1}_{i,j} \delta\Delta\Sigma(\theta_j), \qquad (9)$$
$$\delta\Delta\Sigma(\theta_i) = \Delta\Sigma_o(\theta_i) - \Delta\Sigma_s(\theta_i).$$

When calculating S/N or χ^2, we do not consider the cosmic variance. The χ^2 results for all cases are shown in Fig.11. The upper three panels are for $R_s = 1$ arcmin, and lower panels are for $R_s = 1.5$ arcmin. The left, middle, and right panels are for $z_m = 0.35, 0.435$ and 0.512 respectively. The horizontal axis is Mag_c. The four solid lines in each panel show results for CW1-4 cosmologies, and the dashed lines are for WZ1-2. Among six simulations, CW1 and WZ1 are two different ΛCDM models. From these panels we find:

1. In all the panels, CW2 (w=-0.5) always has the largest χ^2 compared with other cosmologies;

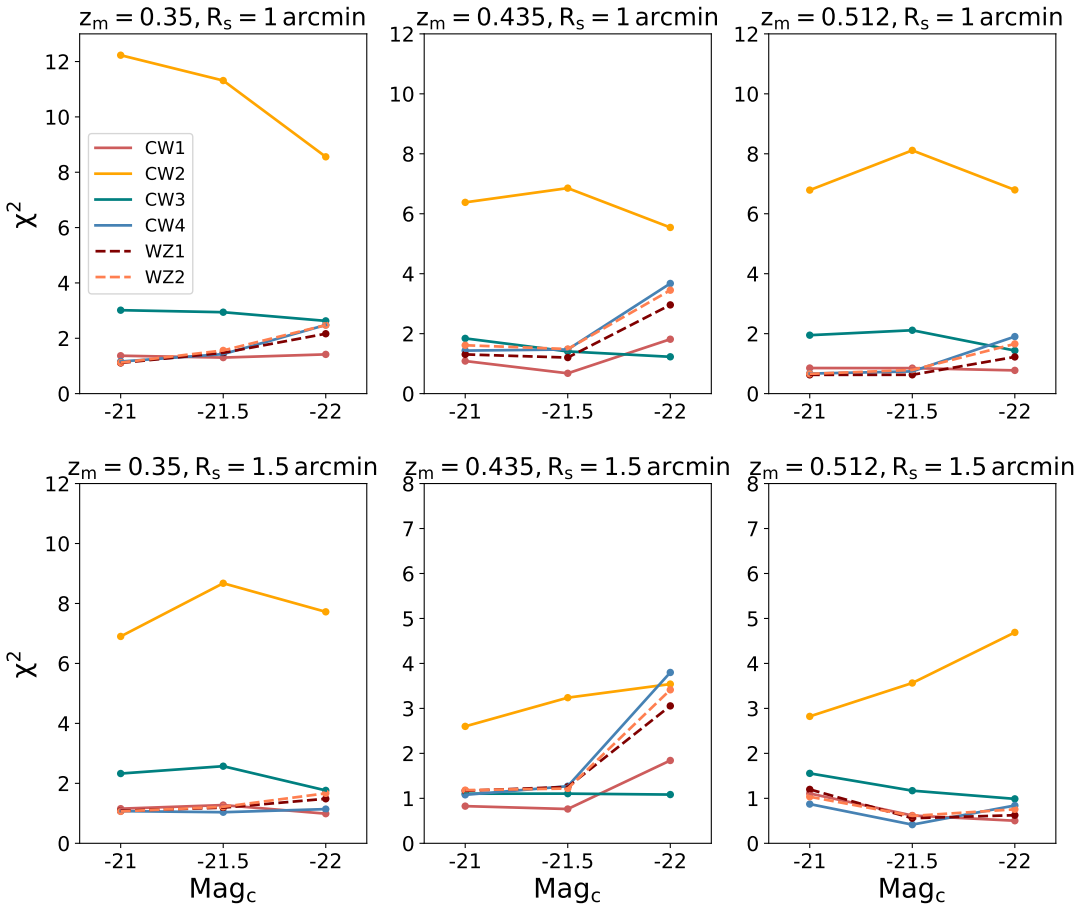

Figure 11. The reduced χ^2 for six cosmologies with different choices of Mag_c, R_s and z_m. The upper three panels are for $R_s = 1$ arcmin, and lower panels are for $R_s = 1.5$ arcmin. The left, middle, and right columns are for $z_m = 0.35, 0.435, 0.512$ respectively. The horizontal axis in each plot is the magnitude cut Mag_c.

2. CW3 (w=-0.8) has the second largest χ^2 in most cases;

3. The other four models, including the two ΛCDM models (CW1,WZ1), the CW4 (w=-1.2) model, and WZ2 (dynamical w(z)), all have comparably low χ^2 i n most cases. The most pronounced exception is in the case of $z_m = 0.435$, $R_s = 1.5$ arcmin, and $Mag_c = -22$, in which the CW3 model yields the lowest χ^2 in contrast.

4. CONCLUSION AND DISCUSSIONS

In this paper we study the stacked lensing signals around the low-density-positions (LDPs), which are defined as places that are devoid of foreground bright galaxies in projection. We show how to define the foreground galaxy population and locate the LDPs in the presence of masks using the CFHTLenS data. Different redshift ranges and magnitude cuts are considered for the foreground population. The measured excess sur-

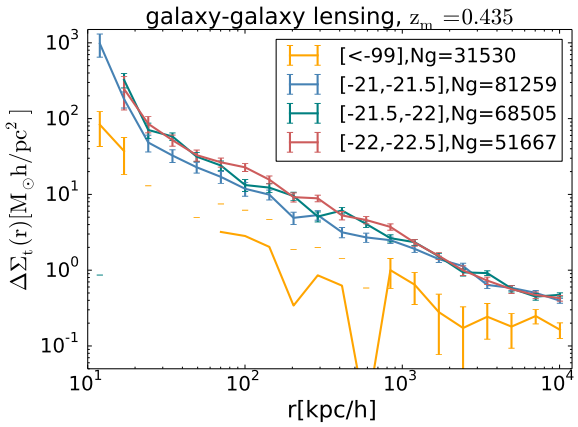

Figure 12. Galaxy-galaxy lensing signals for foreground galaxies in the Magnitude bins of [-21,-21.5], [-21.5,-22], [-22,-22.5] and [< -99], and redshift range of [0.335,0.435]. Ng is the number of foreground galaxies.

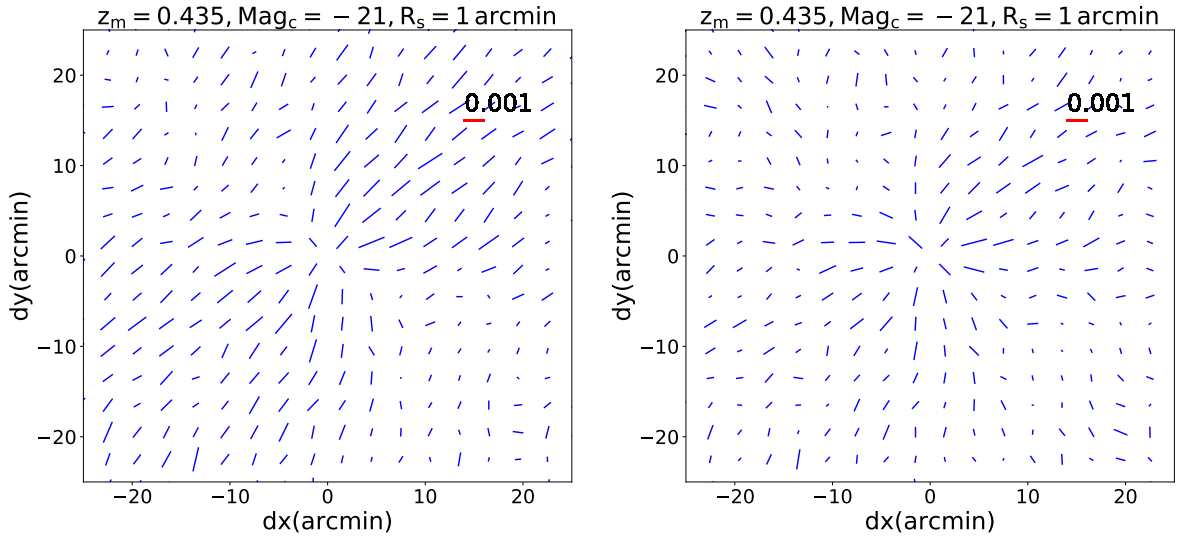

Figure 13. The 2D stacked lensing signals around the LDPs using only the CFHTLenS fields that pass the lensing residual systematics tests. The left panel shows the original result, and the right panel shows results after subtracting the average residual $\overline{\gamma}_{1,2}$. The red line represents the shear strength of 0.001.

face density profiles can be compared with the predictions from simulations. The comparison is made available by drawing correspondence between galaxies and halos/subhalos via SHAM.

With the CFHTLenS shear catalogue, we have successfully measured the lensing signals around the LDPs with a high significance. These measurements are used to constrain dark energy models using simulated galaxies that have similar survey selection effects. We run six cosmological simulations [CW(1,2,3,4) and WZ(1,2)] with different dark energy equations of state, for the purpose of reproducing the mean surface density profile around the LDPs in observation. The cosmological parameters of the six simulations are given in table 1.

Our results of the surface density measurement indicate that the CW2 ($w = -0.5$) and CW3 ($w = -0.8$) models are not favored. The two ΛCDM models (CW1 and WZ1), as well as the CW4 ($w = -1.2$) and WZ2 ($w(z)$ of Zhao et al. (2017)) models, all achieve reasonably good and similar agreement with the observation. The comparisons are made for three foreground redshift bins, three magnitude cuts, and two critical radii for the definition of the LDPs.

There are a number of problems that may impact our results. Here we outline some of them:

4.1. *The Impact of Throwing Away Sources with Absolute Magnitude* $\mathrm{Mag_i}$ *<-99 in the Shear Catalogue*

We show the galaxy-galaxy lensing signals in Fig.12 for foreground galaxies in the redshift range of [0.335,0.435]. The blue, green, red and yellow lines are for galaxies with magnitudes in the range of [-21,-21.5], [-21.5,-22] , [-22,-22.5], and [<-99] respectively. For galaxies of Mag <-99, their lensing signals are quite low, indicating that they likely correspond to less massive sources on average (or even not galaxies). So we think it is safe for us to remove them from the foreground galaxies when generating the LDPs.

4.2. *The Impact of the Fields Which Do Not Pass the Lensing Residual Systematics Tests*

As described in (Heymans et al. 2012), some CFHTLenS fields do not pass the lensing residual systematics tests, which should not be used in shear two-point correlation function. In fig.13, we show the 2D stacked shear patterns around the LDPs using only fields that pass the lensing residual systematics tests. The left panel shows the original result, and the right panel shows results after subtracting the random points signals $\gamma_{\mathrm{rand},1,2}$. The red line represents the shear strength of 0.001. From the right panel we can find that the shear patterns do not change too much from that shown in the lower panel of fig.6, which uses all the fields. For the 1D signals, the conclusion is similar. We therefore simply use the whole CFHTLenS shear catalogue in this work.

4.3. *The Impact of the* σ_8 *When Comparing The Lensing Signals.*

The initial conditions for the CW1-4 simulation are fixed as mentioned in §2.3, supposing the early-time amplitude $\mathrm{A_s}$ is well constrained by the CMB. However, it may be interesting to ask what if we keep the late-time amplitudes the same for these simulations, although

with very different A_s. So we run four new simulations here as a comparison. Three new simulations are run for the CW set, named as CW5,6,7. Also, one new simulation is run for the WZ set, named as WZ3. For CW5,6,7, the parameters $(\Omega_c, \Omega_b, w_{de}, h)$ are set the same as in CW2,3,4 respectively, with the σ_8 being the same as that of CW1. For WZ3, its parameters$(\Omega_c, \Omega_b, w_{de}, h)$ are identical with WZ2, with the σ_8 taken from WZ1. The parameters of the simulations are given in table 2.

All the procedures in §2.3 are repeated for the four simulations. The simulated lensing signals around the LDPs are compared with the observed signals in Fig.14 and Fig.15, which are similar to Fig.9 and 10. The lensing profiles $\Delta\Sigma_s(R)$ for CW5,6,7 are found to be close to each other. Although smaller compared to Fig.9 and 10, discrepancies are still found for some cosmologies between the simulated and observed signals in the lower panels. Their corresponding χ^2 results are shown in Fig.16. The CW5($w = -0.5$) is found to have larger χ^2 than the others in most cases. The χ^2 of CW6($w = -0.8$) seems to be slightly higher than the rest. These results are redshift-dependent, and the least distinguishable case is when $z_m = 0.435$ and $R_s = 1.5$ arcmin, in which different models result in comparable χ^2.

Table 2. Simulation parameters.

Simulation	w_{de}	σ_8	Ω_c	Ω_b	h	n_s
CW5	-0.5	0.85	0.223	0.045	0.71	1
CW6	-0.8	0.85	0.223	0.045	0.71	1
CW7	-1.2	0.85	0.223	0.045	0.71	1
Simulation	w_{de}	A_s	Ω_c	Ω_b	h	n_s
WZ3	w(z)	2.16e-9	0.24188	0.04525	0.702	0.966

We note that our constraints on the dark energy equation of state is still preliminary, in the sense that we have fixed the values of the other cosmological parameters for simplicity. As a next step, we plan to vary the cosmological model with more parameters, and fix those that are best constrained by CMB. We also plan to measure again the LDP lensing signals using the Fourier_Quad method (Zhang et al. 2017, 2018), which is significantly different from the Lensfit method used by the CFHTLenS team. Also, we are looking forward to giving detailed discussions on the redshift evolution of the LDP lensing signals with larger and deeper surveys[7].

ACKNOWLEDGMENTS

This work is based on observations obtained with MegaPrime/MegaCam, a joint project of CFHT and CEA/DAPNIA, at the Canada-France-Hawaii Telescope (CFHT) which is operated by the National Research Council (NRC) of Canada, the Institut National des Sciences de lÚnivers of the Centre National de la Recherche Scientifique (CNRS) of France, and the University of Hawaii. This research used the facilities of the Canadian Astronomy Data Centre operated by the National Research Council of Canada with the support of the Canadian Space Agency.

We thank Gongbo Zhao for providing us parameter tables used for setting the WZ set simulations, Yipeng Jing for providing us one of the CW1 simulation data, and Pengjie Zhang for useful comments. This work is supported by the National Key Basic Research and Development Program of China (No.2018YFA0404504), the National Key Basic Research Program of China (2015CB857001, 2015CB857002), the NSFC grants (11673016, 11433001, 11621303, 11773048, 11403071). JXH is supported by JSPS Grant-in-Aid for Scientific Research JP17K14271. JJZ is supported by China Postdoctoral Science Foundation 2018M632097. LPF acknowledges the support from NSFC grants 11673018, 11722326 & 11333001; STCSM grant 16ZR1424800 & 188014066; and SHNU grant DYL201603.

REFERENCES

Barreira, A., Bose, S., Li, B., & Llinares, C. 2017, JCAP, 2, 031

Behroozi, P. S., Conroy, C., & Wechsler, R. H. 2010, ApJ, 717, 379

Berlind, A. A., & Weinberg, D. H. 2002, ApJ, 575, 587

Brouwer, M. M., Demchenko, V., Harnois-Déraps, J., et al. 2018, MNRAS, 481, 5189

Ceccarelli, L., Padilla, N. D., Valotto, C., & Lambas, D. G. 2006, MNRAS, 373, 1440

Chaves-Montero, J., Angulo, R. E., Schaye, J., et al. 2016, MNRAS, 460, 3100

Clampitt, J., & Jain, B. 2015, MNRAS, 454, 3357

Colberg, J. M., Sheth, R. K., Diaferio, A., Gao, L., & Yoshida, N. 2005, MNRAS, 360, 216

Conroy, C., Gunn, J. E., & White, M. 2009, ApJ, 699, 486

Conroy, C., Wechsler, R. H., & Kravtsov, A. V. 2006, ApJ, 647, 201

[7] https://www.darkenergysurvey.org,https://www.desi.lbl.gov, https://www.lsst.org,http://www.sdss3.org/surveys/boss.php.

Davies, C. T., Cautun, M., & Li, B. 2018, ArXiv e-prints, arXiv:1803.08717
Elyiv, A., Marulli, F., Pollina, G., et al. 2015, MNRAS, 448, 642
Erben, T., Hildebrandt, H., Miller, L., et al. 2013, MNRAS, 433, 2545
Friedrich, O., Gruen, D., DeRose, J., et al. 2018, PhRvD, 98, 023508
Gruen, D., Friedrich, O., Amara, A., et al. 2016, MNRAS, 455, 3367
Gruen, D., Friedrich, O., Krause, E., et al. 2018, PhRvD, 98, 023507
Guo, H., Yang, X., & Lu, Y. 2018, ApJ, 858, 30
Guo, H., Zheng, Z., Behroozi, P. S., et al. 2016, MNRAS, 459, 3040
Guo, Q., & White, S. 2014, MNRAS, 437, 3228
Guo, Q., White, S., Li, C., & Boylan-Kolchin, M. 2010, MNRAS, 404, 1111
Han, J., Frenk, C. S., Eke, V. R., et al. 2012, MNRAS, 427, 1651
Hartlap, J., Simon, P., & Schneider, P. 2007, A&A, 464, 399
Hearin, A. P., Zentner, A. R., Berlind, A. A., & Newman, J. A. 2013, MNRAS, 433, 659
Heymans, C., Van Waerbeke, L., Miller, L., et al. 2012, MNRAS, 427, 146
Hildebrandt, H., Erben, T., Kuijken, K., et al. 2012, MNRAS, 421, 2355
Hoyle, F., & Vogeley, M. S. 2002, ApJ, 566, 641
Huterer, D., & Turner, M. S. 1999, PhRvD, 60, 081301
Jennings, E., Li, Y., & Hu, W. 2013, MNRAS, 434, 2167
Jing, Y. P., Mo, H. J., & Börner, G. 1998, ApJ, 494, 1
Jing, Y. P., Suto, Y., & Mo, H. J. 2007, ApJ, 657, 664
Komatsu, E., Bennett, C. L., Barnes, C., et al. 2014, Progress of Theoretical and Experimental Physics, 2014, 06B102
Lavaux, G., & Wandelt, B. D. 2012, ApJ, 754, 109
Leauthaud, A., Tinker, J., Behroozi, P. S., Busha, M. T., & Wechsler, R. H. 2011, ApJ, 738, 45
Lewis, A., Challinor, A., & Lasenby, A. 2000, Astrophys. J., 538, 473
Li, B. 2011, MNRAS, 411, 2615
Miller, L., Heymans, C., Kitching, T. D., et al. 2013, MNRAS, 429, 2858
Nadathur, S., Hotchkiss, S., Diego, J. M., et al. 2015, MNRAS, 449, 3997
Neyrinck, M. C. 2008, MNRAS, 386, 2101
Niikura, H., Takada, M., Okabe, N., Martino, R., & Takahashi, R. 2015, PASJ, 67, 103
Padilla, N. D., Ceccarelli, L., & Lambas, D. G. 2005, MNRAS, 363, 977
Peacock, J. A. 1999, Cosmological Physics, 704
Perlmutter, S., Aldering, G., Goldhaber, G., et al. 1999, ApJ, 517, 565
Planck Collaboration, Ade, P. A. R., Aghanim, N., et al. 2014, A&A, 571, A1
Platen, E., van de Weygaert, R., & Jones, B. J. T. 2007, MNRAS, 380, 551
Ramos, B. H. F., Pellegrini, P. S., Benoist, C., et al. 2011, AJ, 142, 41
Riess, A. G., Filippenko, A. V., Challis, P., et al. 1998, AJ, 116, 1009
Rodríguez-Puebla, A., Avila-Reese, V., Yang, X., et al. 2015, ApJ, 799, 130
Rodríguez-Puebla, A., Primack, J. R., Avila-Reese, V., & Faber, S. M. 2017, MNRAS, 470, 651
Sánchez, C., Clampitt, J., Kovacs, A., et al. 2017, MNRAS, 465, 746
Simha, V., Weinberg, D. H., Davé, R., et al. 2012, MNRAS, 423, 3458
Springel, V. 2005, MNRAS, 364, 1105
Springel, V., & Hernquist, L. 2002, MNRAS, 333, 649
Taylor, A., Joachimi, B., & Kitching, T. 2013, MNRAS, 432, 1928
Vale, A., & Ostriker, J. P. 2004, MNRAS, 353, 189
—. 2006, MNRAS, 371, 1173
van den Bosch, F. C., Yang, X., Mo, H. J., et al. 2007, MNRAS, 376, 841
Wechsler, R. H., & Tinker, J. L. 2018, ArXiv e-prints, arXiv:1804.03097
Weinberg, D. H., Mortonson, M. J., Eisenstein, D. J., et al. 2013, PhR, 530, 87
Yang, X., Mo, H. J., & van den Bosch, F. C. 2003, MNRAS, 339, 1057
Yang, X., Mo, H. J., van den Bosch, F. C., Zhang, Y., & Han, J. 2012, ApJ, 752, 41
Yang, X., Zhang, Y., Wang, H., et al. 2018, ApJ, 860, 30
Zehavi, I., Zheng, Z., Weinberg, D. H., et al. 2011, ApJ, 736, 59
Zhang, J., Zhang, P., & Luo, W. 2017, ApJ, 834, 8
Zhang, J., Dong, F., Li, H., et al. 2018, ArXiv e-prints, arXiv:1808.02593
Zhao, C., Tao, C., Liang, Y., Kitaura, F.-S., & Chuang, C.-H. 2016, MNRAS, 459, 2670
Zhao, G.-B., Raveri, M., Pogosian, L., et al. 2017, Nature Astronomy, 1, 627
Zheng, Z., Berlind, A. A., Weinberg, D. H., et al. 2005, ApJ, 633, 791
Zu, Y., & Mandelbaum, R. 2016, MNRAS, 457, 4360

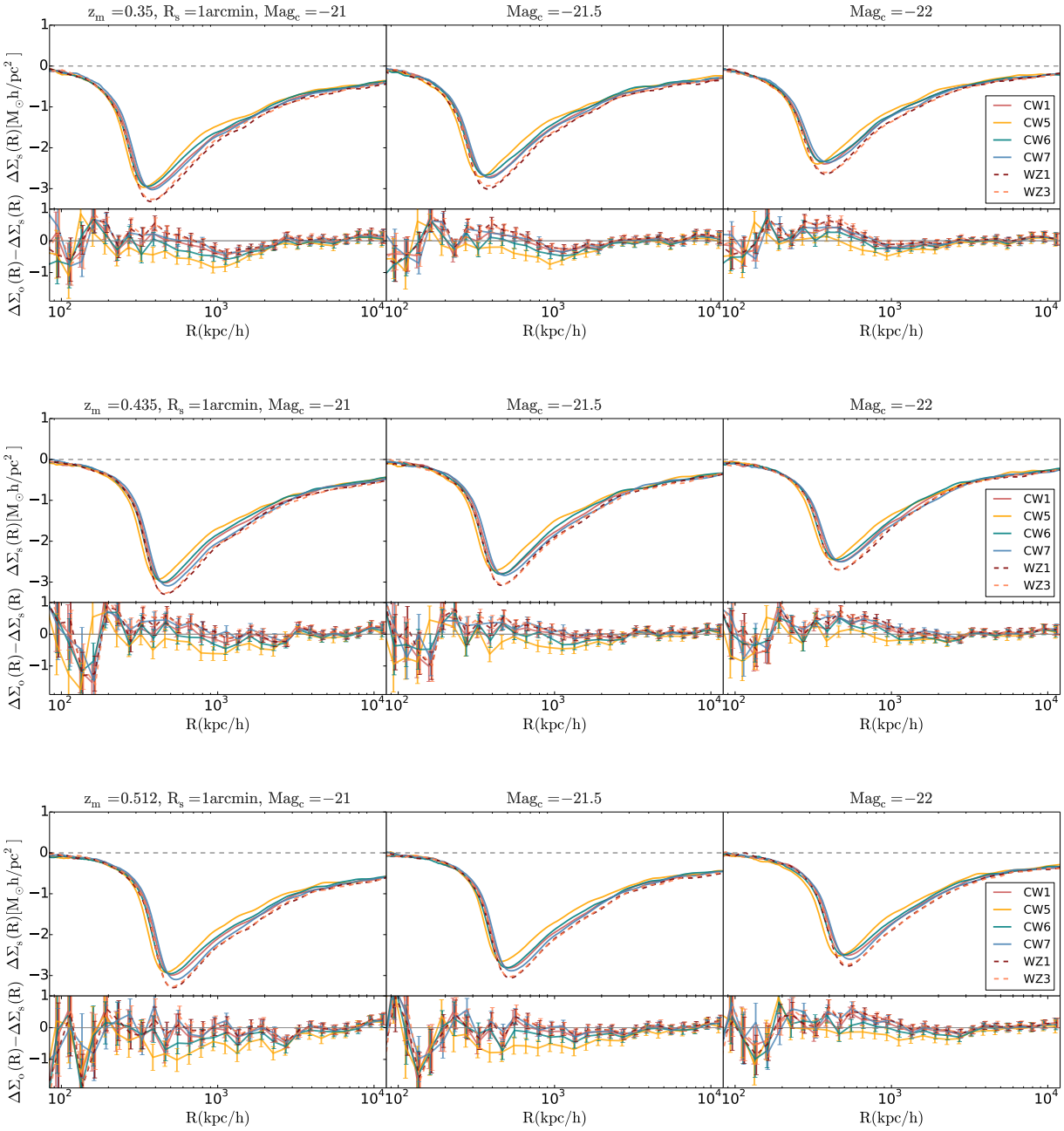

Figure 14. Similar to Fig.9, but with a new set of simulations described in §4.3. CW5,6,7 all share the same σ_8 as that of CW1, and WZ3 has the same σ_8 as that of WZ1.

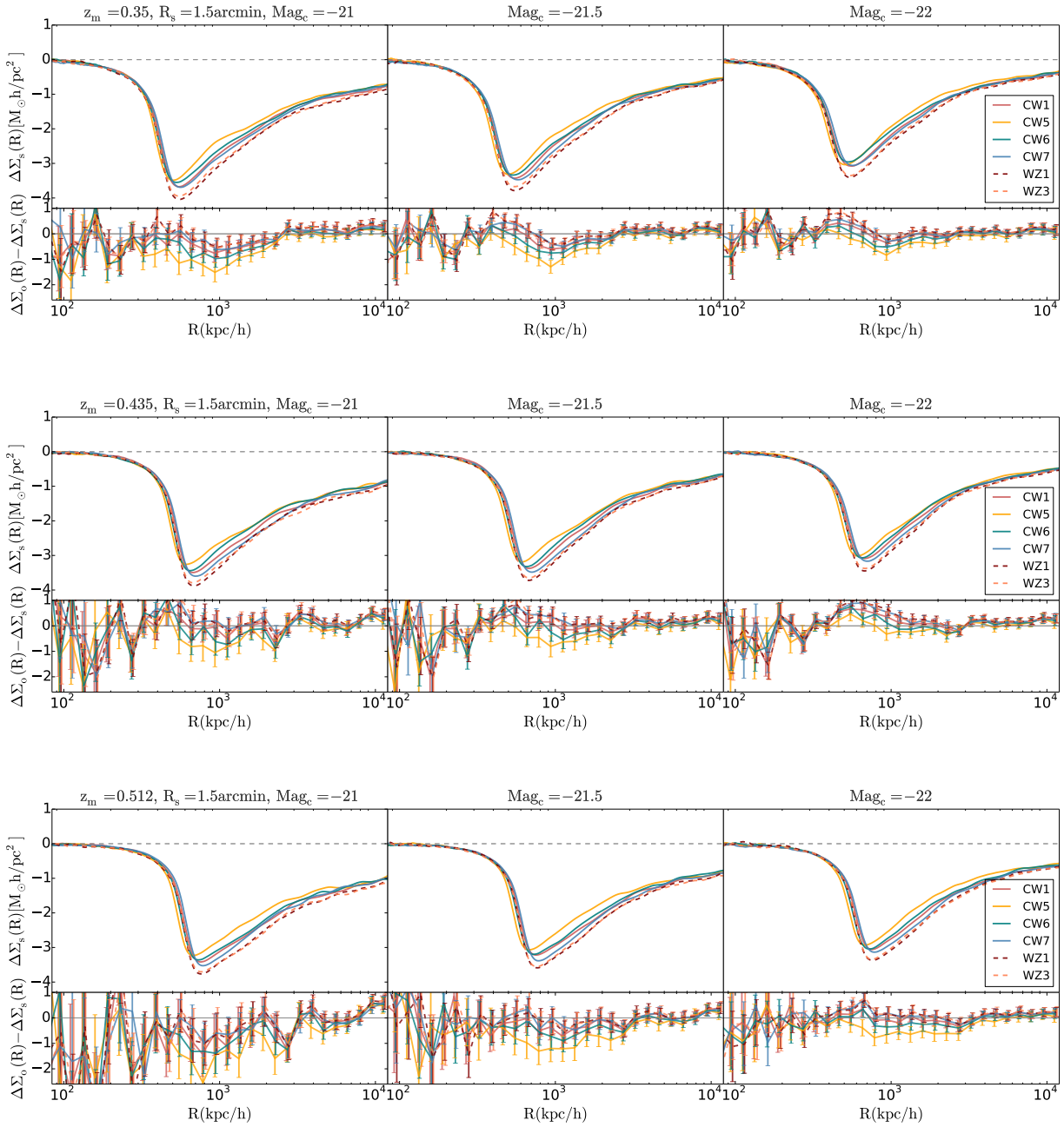

Figure 15. Similar to fig.14, but with $R_s = 1.5$ arcmin.

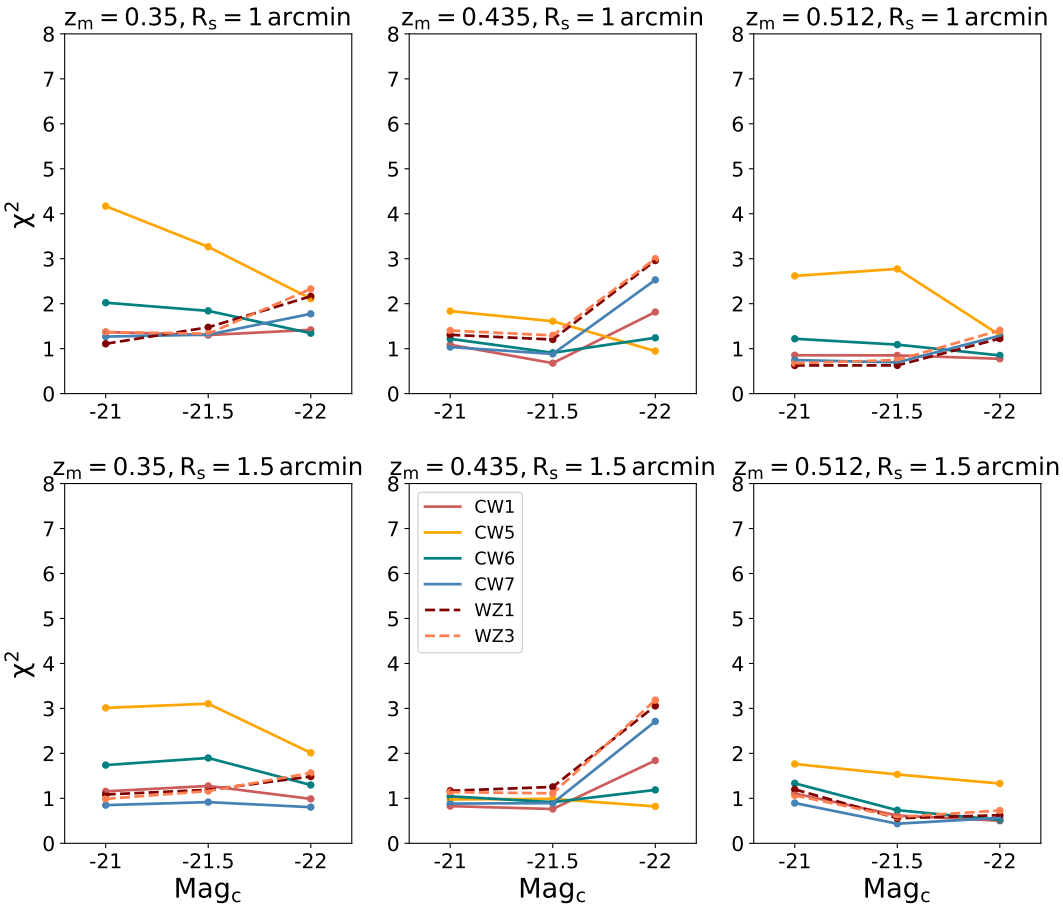

Figure 16. Simalar to Fig.11, but with a new set of simulations described in §4.3. CW5,6,7 all share the same σ_8 as that of CW1, and WZ3 has the same σ_8 as that of WZ1.